Terrestrial Laser Scanning of Anthropogenic Beach Berm Erosion and Overtopping

Authors: Schubert, Jochen E., Gallien, Timu W., Majd, Morteza Shakeri, and Sanders, Brett F.

Source: Journal of Coastal Research, 31(1) : 47-60

Published By: Coastal Education and Research Foundation

URL: https://doi.org/10.2112/JCOASTRES-D-14-00037.1

Journal of Coastal Research	31	1	47–60	Coconut Creek, Florida	January 2015

Terrestrial Laser Scanning of Anthropogenic Beach Berm Erosion and Overtopping

Jochen E. Schubert[†], Timu W. Gallien[†‡], Morteza Shakeri Majd[†], and Brett F. Sanders[†]*

[†]Department of Civil and Environmental Engineering
University of California, Irvine
Irvine, CA 92697, U.S.A.

[‡]Scripps Institution of Oceanography
University of California, San Diego
La Jolla, CA 92093, U.S.A.

www.cerf-jcr.org

www.JCRonline.org

ABSTRACT

Schubert, J.E.; Gallien, T.W.; Majd, M.S., and Sanders, B.F., 2015. Terrestrial laser scanning of anthropogenic beach berm erosion and overtopping. *Journal of Coastal Research,* 31(1), 47–60. Coconut Creek (Florida), ISSN 0749-0208.

Anthropogenic berms are widely deployed to manage coastal flooding. The dynamic erosion of scraped berms exposed to waves and a rising tide in southern California was monitored with a terrestrial laser scanner (TLS) on three occasions in February and March of 2012. An improved characterization of initial berm geometry and the dynamics of berm erosion was pursued to accurately predict the onset and impact of coastal flooding associated with berm erosion and overtopping. TLS is shown to yield a digital terrain model (DTM) with a vertical accuracy of *ca*. 3 cm, indicating it is an excellent source of data for initializing mechanistic and/or empirical models that could be used to predict the onset and rate of wave overtopping. Minimum scan point spacings required to achieve this level of accuracy are investigated and reported. Additionally, a dimensionless water level representing the fractional submergence of the berm is identified as a good predictor of cumulative berm erosion under the test conditions.

ADDITIONAL INDEX WORDS: *Coastal flooding, urban flooding, sea level rise, flood prediction*.

INTRODUCTION

Anthropogenic berms refer to a mechanically constructed ridge of sand positioned on the crest of the natural beach profile. Sand (0.2–0.5 m) is typically scraped from the foreshore and deposited on the beach crest (Bruun, 1983). Anthropogenic berms may be constructed in the days and hours before an anticipated marine flood event, such as an extreme high tide or an energetic swell event; on a seasonal basis in anticipation of the storm season; and on a continual basis to maintain or strengthen persistent berms. The practice originated primarily as an erosion-control strategy (*e.g*., Bruun, 1983; McNinch and Wells,1992; Tye, 1983; Wells and McNinch, 1991) and has been widely deployed as a coastal management technique along the U.S. eastern and Gulf coasts (Clark, 2005; Kratzmann and Hapke, 2012; Wells and McNinch, 1991), in Australia (Carley *et al*., 2010), and in Europe (Harley and Ciavola, 2013; Rogers *et al*., 2010). Gallien *et al*. (unpublished data) report three distinct types of berming in the southern California bight, based on deployment duration: event, seasonal, and persistent. Event berms are triangular in cross section, extend 60–600 m in the alongshore direction, and exhibit both the lowest volume (~4 m^3/m) and average crest elevations (~5 m North American Vertical Datum of 1988 [NAVD88]) of all berms studied. Seasonal berms extend 70–980 m alongshore, are 6–28 m^3/m in volume, and have an average crest elevation from 5.3 m to 6.4 m NAVD88. The largest, longest, and highest of all berms in the southern California bight protects the Naval Amphibious Base, Coronado in San Diego and averages 48 m^3/m in volume, 1.2 km in length, and nearly 7 m NAVD88 in mean crest elevation. Event berms and seasonal berms in the region are considerably smaller in length, height, and width than those constructed along the Atlantic and Gulf coasts (Gallien *et al*., unpublished data). Examples of event-type berming at Newport Beach, California, are shown in Figure 1. Note from Figure 1 that berms are sometimes constructed from the shoreward side, particularly if access to the beach foreshore is restricted.

Berms are constructed in southern California primarily to guard against coastal flooding into urban lowlands, where significant damages would follow. Here coastal flooding is driven by a combination of factors, including high astronomical tides, waves, storm surge, and other fluctuations such as those caused by the El Niño Southern Oscillation (ENSO) (Cayan *et al*., 2008). More frequent and damaging storms resulting from the combination of higher sea levels, storm surge, high tides, and waves are expected to test the limits of coastal flood defenses (Strauss *et al*., 2012). Tebaldi, Strauss, and Zervas (2012) conclude that southern California is among the most sensitive areas of the United States to changes in sea level: today's 100 year coastal flood will become an annual occurrence by the year 2050. Additionally, a statewide impact assessment indicates that a wide range of critical infrastructure—including 5600 km of roadways, 450 km of railways, 29 wastewater treatment facilities, and countless buildings and their contents valued at over $100 billion—will be at risk of coastal flooding by 2100, based on 1–1.4 m in sea level rise (Heberger *et al*., 2009). Globally, over 20 million people reside below present high-tide levels, and as many as 200 million are vulnerable to flooding during extreme events (Nicholls, 2010, 2011). Concomitant pressures of urbanization and climate change point to significant increases in the vulnerability of major international port cities to flooding. Population exposure is expected to triple, whereas a tenfold increase in asset exposure totaling 9% of

DOI: 10.2112/JCOASTRES-D-14-00037.1 received 13 February 2014; accepted in revision 30 March 2014; corrected proofs received 16 May 2014; published pre-print online 4 June 2014.
*Corresponding author: bsanders@uci.edu

Figure 1. Anthropogenic berms such as these are constructed in the days and hours before an anticipated flood event in Southern California; they have been termed "event-type berms" by Gallien *et al.* (2014). (Color for this figure is available in the online version of this paper.)

global gross domestic product is anticipated (Hanson *et al.*, 2011).

In the short term, accurate mapping of coastal flooding is critical for anticipating and mitigating flood vulnerabilities and responding to emergencies (National Research Council Staff, 2009). In urban lowlands, hydraulic models have been successfully used to map flood impacts driven by extreme high tides and storm surge (Bates *et al.*, 2005; Brown, Spencer, and Moeller, 2007; Dawson *et al.*, 2009; Knowles, 2010; Martinelli, Zanuttigh, and Corbau, 2010; Purvis, Bates, and Hayes, 2008; Smith, Bates, and Hayes, 2012; Wadey, Nicholls, and Hutton, 2012), but predictive skill has been limited by uncertainties in wave-driven overtopping volumes (Wadey, Nicholls, and Hutton, 2012). Recent research suggests that wave statistics, including significant wave height and period, can be combined with relatively simple beach parameters such as slope and freeboard to empirically estimate the overtopping flows (Gallien, Sanders, and Flick, 2014; Laudier, Thornton, and MacMahan, 2011). Such data can then be input into hydraulic models as a line source (along the inland crest of a beach berm) to simulate resulting patterns of urban flooding, as shown by Gallien, Sanders, and Flick (2014). Alternatively, coupled hydromorphological models (*e.g.*, Figlus *et al.*, 2011; Harley and Ciavola, 2013; Roelvink *et al.*, 2009; van Rijn, 2009; Vousdoukas *et al.*, 2012; Zhu and Dodd, 2013) may prove capable of describing beach change and overwash volumes sufficient for coastal flood prediction. Flood mapping by planar extrapolation of wave runup heights, while far easier and proven for mapping flood zones along many shorelines, is unfortunately inadequate for urban lowlands (Bates *et al.*, 2005; Gallien, Sanders, and Flick, 2014; Gallien *et al.*, 2013). Generally, there is a lack of field data characterizing berm performance during storms and the impacts of berm failure on the timing and distribution of coastal flooding.

This paper presents the results of a field campaign to document the initial conditions and dynamic erosion of anthropogenic berms using terrestrial laser scanning (TLS). TLS is increasingly applied for studies of beaches (Feagin *et al.*, 2014) and has been combined with video analyses for wave-by-wave studies of morphodynamics (Vousdoukas *et al.*, 2014). On three occasions in February and March of 2012, a prototype berm was constructed on the foreshore of Newport Beach at low tide, scanned to document its initial shape, and then scanned in near-continuous fashion with the rising tide to document subsequent erosion. The purpose was twofold: (1) to measure the performance of the TLS system relative to accuracy and assess strengths and drawbacks that are likely to bear on the suitability of this technology to support flood prediction, and (2) to obtain a better understanding of the resilience of anthropogenic berms to erosion and overtopping when exposed to a rising tide and waves. In particular we seek an understanding of basic mechanisms by which the berm is eroded and a deeper understanding of the rate of erosion and the factors controlling it. More broadly we seek to promote improved predictions of coastal flooding in urban lowlands.

The study site is adjacent to Newport Pier in the city of Newport Beach, California, approximately 70 km SE of central Los Angeles (see Figure 2). The pier is located on Balboa Peninsula, which separates the Pacific Ocean from Newport Bay, and is positioned at a break in the strike of the shoreline. Upcoast of the pier, where berm experiments are performed, the beach faces WSW (236° from N), and downcoast the beach faces SSW (196° from N).

Lower Newport Bay is densely developed and features an active pleasure craft harbor, as shown in Figure 2, while the upper bay is a nature preserve with extensive saltwater wetlands (not shown in Figure 2). Areas bordering the lower

Figure 2. Berm experiments were conducted adjacent to Newport Pier in Newport Beach, California. Berms were constructed at low tide and exposed to runup and waves. The location of wave and pressure measurements (using AWAC) is shown. (Color for this figure is available in the online version of this paper.)

bay are vulnerable to flooding, particularly Balboa Island and Balboa Peninsula. Sheltered from significant wave action, Balboa Island floods when high embayment levels overtop concrete flood defenses, whereas the peninsula may flood from high embayment levels or wave runup and overtopping of the beach (Gallien, Sanders, and Flick, 2014; Gallien, Schubert, and Sanders, 2011; Gallien *et al*., 2013). Temporary event-type berms are deployed along the ocean-facing portion of Newport Beach to mitigate flooding threats from the coincidence of high tides and long period swell. Ocean levels at Newport are influenced by astronomical tides ranging between 1–2.7 m (NAVD88, tidal epoch 1983–2001 at Newport Bay entrance), storm surge, El Niño thermal expansion, and wave setup, which under extreme conditions may superelevate astronomical tidewater levels by a further 0.5 m (Flick, 1998).

METHODS

Prototype berms were constructed on three dates: 21 February 2012 (berm 1), 7 March 2012 (berm 2), and 20 March 2012 (berm 3). These dates correspond to the availability of city personnel and a sufficiently large intertidal range to facilitate berm construction, *i.e*. a low tide that creates access to the foreshore and a high tide that ensures complete erosion of the berm. In practice berms may be constructed over several kilometers of shoreline in advance of a storm, but only a berm of limited length was possible here due to construction and scanning limitations. The prototype design was modeled after event-type berms used throughout the region and consisted of a central section parallel to the shoreline, *ca*. 16 m long and 2 m high, flanked by 8 m long angled walls, as shown in Figure 3. This design guards the back side of the berm from flooding during the initial stages of attack and prolongs the duration over which the berm is eroded exclusively from its ocean-facing side.

The berm was constructed with a front-end loader (Model 624J, John Deere, Moline, Illinois, U.S.A.) operated by a City of Newport Beach employee. The loader scraped sandy material immediately inland (berms 1 and 2) or seaward (berm 3) of the berm. Survey stakes around the intended footprint of the berm guided placement of the sand. Similar to berm erosion field experiments conducted by Fisher, Overton, and Chisholm (1986) at Duck, North Carolina, the berm toe was placed at approximately mean sea level (0.8 m above NAVD88). During low tide, initial front and back terrestrial laser scans were performed, and the digital camera was positioned on Newport Pier. A real-time kinematic (RTK)–global positioning system (GPS) receiver provided real-time elevation data for accurate vertical positioning of the berm on the beach face, as described in the next section. No compaction or profiling of the berm was attempted. The deposited material was left unconsolidated with front and back slope angles ranging from 32°–37°, which are typical values for damp sand. The median grain size of the sandy beach material (D_{50}) was analyzed for each constructed berm and found to be uniformly 0.42 mm. Resulting berm heights and cross-shore widths for the central berm section (parallel to the shoreline) were as follows: berm 1, 1.3 m high, 3.0 m wide; berm 2, 1.4 m high, 3.7 m wide; and berm 3, 1.8 m high, 4.5 m wide.

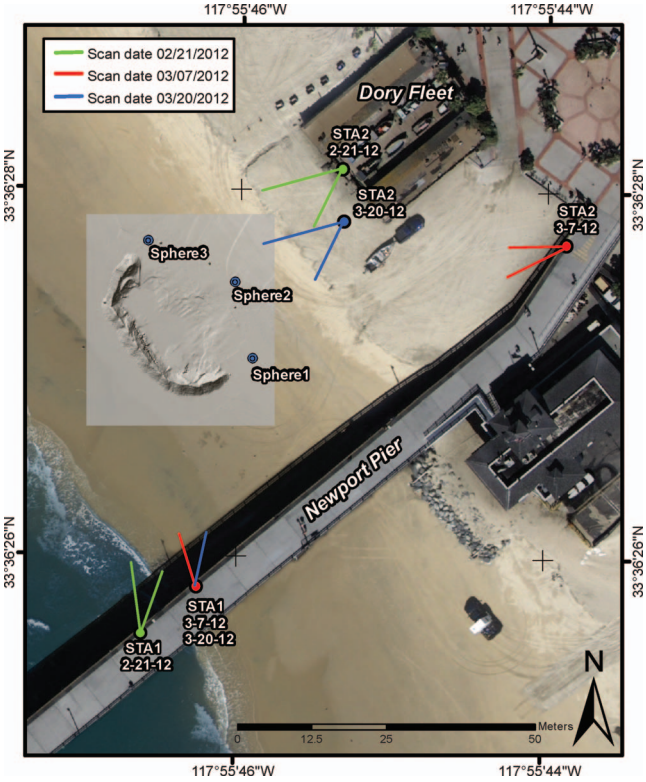

Figure 3. Berms were constructed next to Newport Pier to enable continuous scanning and time-lapse photography with an onshore perspective (front scan). Scans with an offshore perspective (back scans) were also completed to build a three-dimensional point cloud of each berm, and survey spheres (shown) were deployed to merge front and back scans in a postprocessing step. (Color for this figure is available in the online version of this paper.)

RTK-GPS Survey

A ProMark3 geodetic survey receiver using the global positioning system (Magellan, Santa Clara, California, U.S.A.) was used to georeference the TLS, guide berm construction, measure beach slopes, and provide control points to measure the accuracy of the TLS data. In stand-alone mode, the ProMark3 has point accuracy of ~3 m. When receiving corrections, however, the unit can operate in RTK mode and produce centimeter accuracies in both horizontal and vertical directions. To receive real-time corrections, the GPS unit was linked wirelessly to base station FVPK of the Orange County Real Time Network (OCRTN), with a baseline length of 5 km. The OCRTN provides corrections better than 2 cm in the horizontal and 4 cm in the vertical (Orange County Public Works, 2014). Each RTK-GPS observation consists of x, y, and z information referenced to the North American Datum of 1983 (NAD83) and NAVD88. Survey points were collected on the relatively flat foreshore around the perimeter of the berm, and additional points were collected on the foreshore and in waist-deep water at low tide to measure the foreshore beach slope.

Berm Scanning

Terrestrial laser scanning, or LIDAR (light detection and ranging), has emerged as a valuable technology for capturing

Figure 4. Photographs of berm 2 at (left to right) 1700, 1800, and 1830 show the progressive rise of the tide and erosion of the berm that occurred in each of the three experiments. (Color for this figure is available in the online version of this paper.)

the three-dimensional geometry of complex objects ranging from forests to industrial facilities (Vossman and Maas, 2010). Aerial laser scanning has yielded high-resolution digital terrain models (DTMs) that support a new class of detailed and accurate flood models (Bates, 2012), as well as numerous studies of beach dynamics (*e.g.*, Brock *et al.*, 2002; Sallenger *et al.*, 2003; Yates *et al.*, 2008). TLS data has been shown to enhance the local precision of urban flood predictions by mapping features such as sidewalks and street surface camber (Sampson *et al.*, 2012); this could prove invaluable for coastal flood prediction by allowing for quick mapping of beach topography before an imminent flood threat and reducing uncertainties. TLS systems can be used for more detailed morphodynamic studies (*e.g.*, Feagin *et al.*, 2014), and TLS systems on mobile platforms (*e.g.*, Barber and Mills, 2007; Bitenc *et al.*, 2011; Sampson *et al.*, 2012) could enable a beach scan over the scale of a city in a matter of hours, although extreme care would be required for a high level of accuracy, *e.g.*, 1–5 cm. Topographic accuracies in this range have proven necessary to predict the onset of overtopping for weirlike overflow events (Gallien, Schubert, and Sanders, 2011).

A GX3D TLS (Trimble Navigation Limited, Sunnyvale, California, U.S.A.) was used for berm scanning. The system relies on a pulsed laser to sample the three-dimensional properties of surfaces and objects. The Trimble unit allows for 360° horizontal and 60° vertical continuous scanning and has a maximum optimal scan range of 200 m. Scanned relative point accuracy is dependent on scan range, and for this project laser scanning was undertaken at a distance of less than 100 m, allowing for a best system-scan accuracy of <7 mm. During station setup the GX3D was manually leveled within 0.001°, and an inbuilt, dual-axis tilt compensation system with automatic leveling allowed for correction of level drift, which may occur from system vibration or settling, within a $\pm 0.25°$ range. The measured output consists of a data-point cloud, in which each point is attributed with an easting, northing, orthometric elevation as well as a pulsed laser reflection intensity. The GX3D uses a pulsed 532 nm (green) laser that is not designed to penetrate water; thus measurements over water surfaces such as the swash zone may be difficult to interpret. While reflection intensity depends on many factors, it is inversely related to the presence of water and thus can help to identify water lines on the beach.

Front (STA1) and back (STA2) terrestrial laser scans were completed immediately after berm construction on each of the three test dates to characterize initial berm geometry. Locations for STA1 and STA2 were varied across the three study dates for the best possible scan coverage, considering the location of the berm and line-of-sight obstructions such as maintenance vehicles. Locations of STA1 and STA2 and approximate survey sphere placements used for automatic georeferenced merging of front and back scans are shown in Figure 3. The geodetic locations of STA1 and the survey spheres were surveyed using RTK-GPS and converted to NAD83 and NAVD88. While an assessment of the GPS vertical accuracy was not conducted on each survey day, a previous test at this site with the same equipment yielded a vertical accuracy of 1.4 cm (Gallien, Schubert, and Sanders, 2011). All point clouds were georeferenced using STA1, and survey spheres corrected RTK coordinates as control points. The TLS was set to scan using a maximum resolution of 7.5 cm at the furthest distance (STA1), and the scan interval was proportionally smaller at shorter distances. This resolution was chosen so each scan would take 3–5 minutes.

Following the initial front and back scans, front scanning with the TLS continued with the rise of the tide and progressive erosion of the berm. Actual scan times varied between 3 and 16 minutes, with an average scan interval of 6 minutes. Variability in the scan interval was due to scanner self-calibration, which occurred automatically when heavy wind gusts unsettled the TLS.

Time-Lapse Photography

A Powershot G12 photo camera (Canon U.S.A., Melville, New York, U.S.A.) was used during each geodetic survey to capture digital images of the beach berm at 1 minute time intervals. The camera was tripod mounted and the shutter was triggered automatically using a shutter release unit. The images were time stamped and used to produce an optical time-lapse series of the berm erosion process. An example of the captured photos can be seen in Figure 4.

Berm Data Processing

The georeferenced point clouds of merged front and back scans were combined into a single point cloud representative of the initial conditions. Subsequent front scans combined with the initial back scan characterize the time-dependent geometry

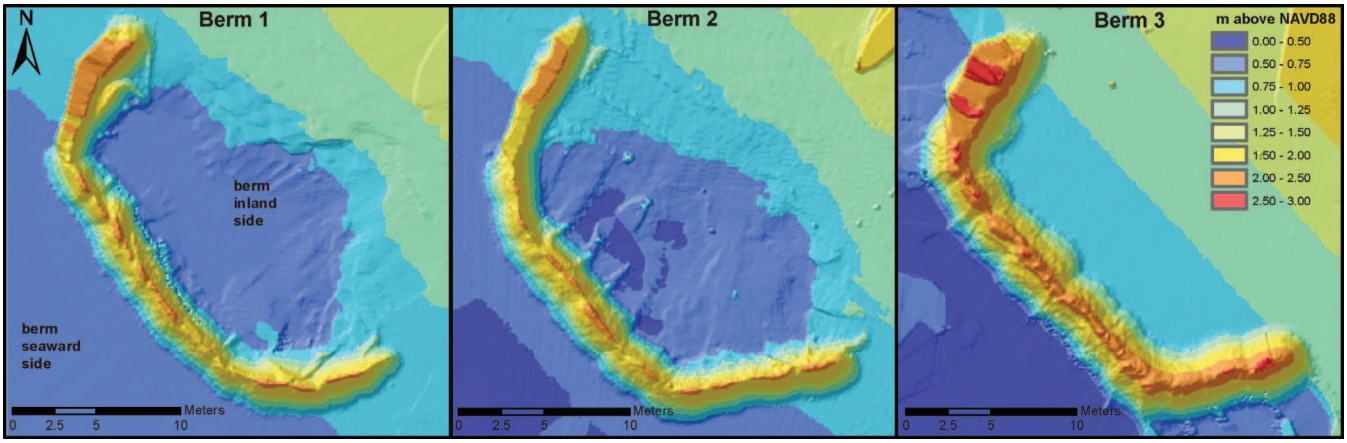

Figure 5. DTMs show that the geometry and orientation of berms 1, 2, and 3 were similar, and that berm 3 was the highest of the three. (Color for this figure is available in the online version of this paper.)

of the berm; eroded portions of the berm visible in the back scan, however, must be removed. This primarily affects point clouds corresponding to advanced stages of erosion. A processing workflow was established using ArcMap 10.0 (Esri, Redlands, California, U.S.A.) to eliminate eroded back scan points based on the intersection of the coverage area of front scan points. After creating a series of point clouds corresponding to different times, a 7.5 cm resolution DTM was created using inverse distance weighting (IDW) interpolation. Examples of the generated berm DTMs for each survey day are shown in Figure 5. Reflected TLS intensity was recorded and processed along with surface elevations to enable studying of beach surface characteristics under rising tide and wetting berm surface conditions. The uncalibrated reflectance intensity was also interpolated to a 7.5 cm resolution raster grid using IDW interpolation. An example of berm-reflected intensity in intensity units (iu) over time is shown in Figure 6.

Sand volumes for each berm scan were calculated using a raster model of the berm height, measured relative to the sloping foreshore. A DTM of the sloping foreshore was created by removing berm object points from each LIDAR point cloud and again applying IDW interpolation onto the same 7.5 cm resolution raster grid. The berm height model was computed by subtracting the foreshore DTM from the original DTM. Volumes were then calculated in ArcMap 10.0 above the zero-elevation reference plane. Percent erosion was computed by subtracting the berm volume of each scan from the initial volume and normalizing by the initial volume. The berm height raster models were also used to extract cross-sectional and alongshore profiles of the berms at each time step.

Alongshore profiles of the berm crest and berm toe were identified by computing a raster model of the berm slope and contouring slope values, which clearly showed the crest and toe positions, as shown in Figure 7. Crest and toe polylines were

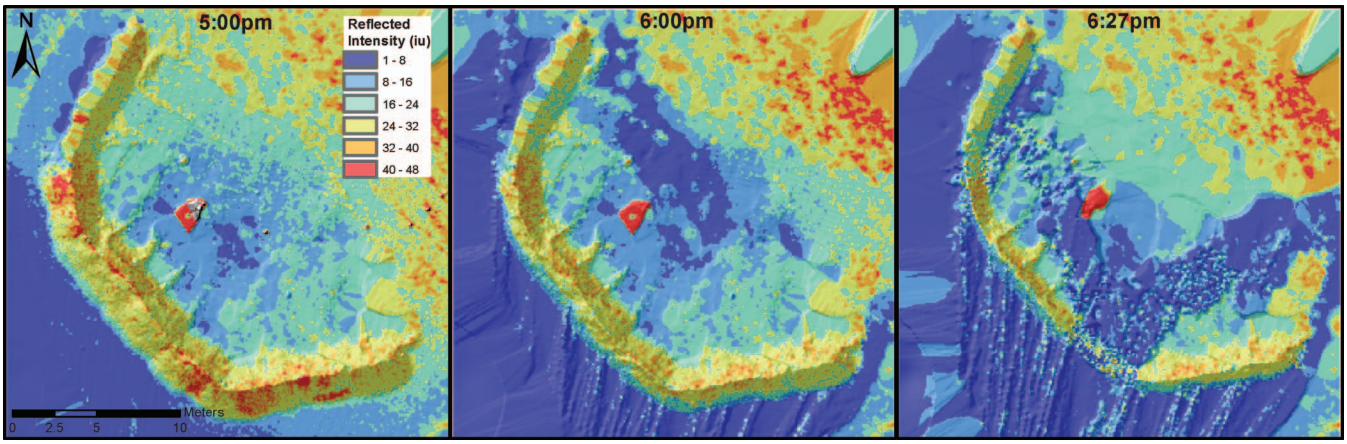

Figure 6. The LIDAR intensity reveals the interface between water and subaerial sand because the return from water corresponds to low intensity. (Color for this figure is available in the online version of this paper.)

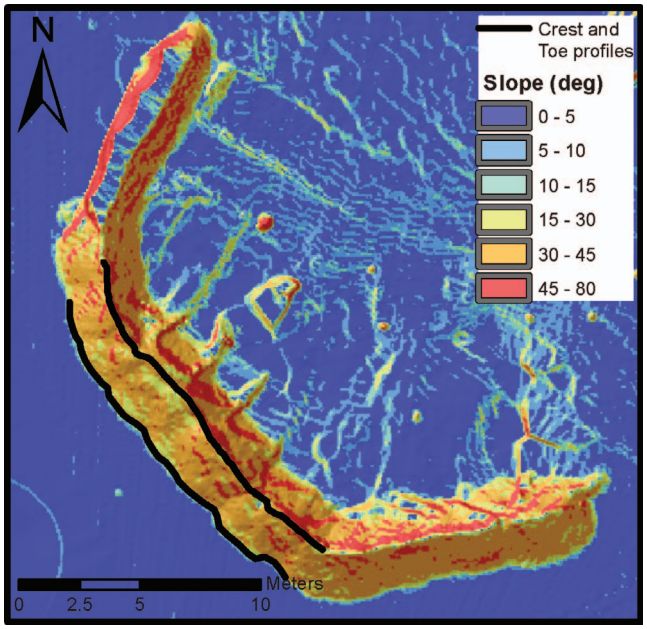

Figure 7. Polylines were etched along the toe and crest of each berm to extract average toe and crest elevations, as well as minimum crest elevations, as shown here for berm 2. (Color for this figure is available in the online version of this paper.)

then traced manually, and elevations along the line were extracted at approximately 10 cm intervals. Separate polylines were saved for each time step in which a noticeable change occurred in toe or crest shape. Average toe elevation, average crest elevation, and minimum crest elevation were saved for each time step for subsequent analysis. It is noted that the reported berm toe elevation may be higher than the actual toe elevation toward the end of each berm experiment because the pulse LIDAR cannot penetrate water to measure a submerged toe elevation. Toward the end of each experiment, errors in the reported toe elevations may be in the 5–10 cm range, while errors during the initial stages of berm erosion are likely less than 3 cm.

The preceding polylines were also used to extract crest-averaged and toe-averaged LIDAR intensity data at each time step. An advantage of this averaging is the removal of "salt and pepper" noise caused by a combination of scan pattern, receiver automatic gain adjustments, and laser reflection angle, as well as material properties of the reflecting surface (Chust *et al.*, 2008; Nobrega, Quintanilha, and O'Hara, 2007).

Wave and Pressure Measurements

An acoustic wave and current (AWAC) profiler wave/current gage (Nortek AS, Rud, Norway) was deployed in approximately 10 m of water and 300 m directly offshore of the berm to measure directional wave properties and pressure. The instrument was deployed in early January 2012 and collected data for a period exceeding 3 months. The AWAC operates in stand-alone mode with an external battery for power and internal memory for data recording. Wave height accuracies are stated to be less than 1%, and pressure resolution and absolute accuracies are less than 0.005% and 0.1%, respectively, of the total depth. This corresponds to a resolution and accuracy of 0.05 cm and 1 cm, respectively, based on the 10 m water depth. The AWAC measured waves at the top of every hour using a 17 minute burst window at a rate of 4 Hz. Pressure was sampled at 1 Hz every 10 minutes for a 2 minute period. Wave measurements were processed using Storm commercial processing software (Nortek U.S.A., Boston, Massachusetts, U.S.A.), and results are shown in Table 1.

Pressure data was processed to fill hourly data gaps, remove high-frequency variability, and reference the resulting time series to NAVD88. Data gaps were filled using piecewise cubic Hermitian interpolation with MATLAB (MathWorks, Natick, Massachusetts, U.S.A.), and the resulting time series was low-pass filtered in the frequency domain to resolve variability at periods longer than 2 hours, including the dominant modes at diurnal and semidiurnal periods. We used 6 minute National Oceanic and Atmospheric Administration tide measurements at Los Angeles (35 km to the NW) to reference the pressure data to NAVD88. A variable offset (correction) was computed by subtracting a running fortnightly average pressure (depth) from a running fortnightly average Los Angeles tide height referenced to NAVD88; this was resampled every 10 minutes by interpolation for consistency with the 10 minute pressure data. The offset/correction was then added to the low-pass–filtered pressure data to yield a local time series of water height relative to NAVD88. A variable offset was used to account for settling of the instrument over time by 5–10 cm, which was revealed by an increasing trend in the fortnightly pressure averages over the deployment period when fortnightly tide averages at Los Angeles and La Jolla (130 km to the SE) exhibited a weaker but decreasing and coherent trend. That is, the fortnightly tide height average at Los Angeles and La Jolla tracked very closely with maximum differences of 2.35 cm and average differences of 0.58 cm. Hence, we have assumed that the running (every 10 min) fortnightly average of the Newport Pier and Los Angeles tides remain equal, giving a Newport tide record referenced to NAVD88 with a maximum error of 2.35 cm, based on the Los Angeles/La Jolla comparison. The offset/correction was –10.78 m, –10.80 m, and –10.79 m coincident with experiments for berms 1, 2, and 3, respectively.

Wave Setup and Runup Estimates

Wave setup and runup were calculated to characterize water levels at the berm face in relation to datum-referenced water heights outside the surf zone, as described above. Based on the beach slopes and wave properties shown in Table 1, the Iribarren number ξ, setup $\langle\eta\rangle$, and runup R_2 (2% exceedance probability) were computed in accordance with Stockdon *et al.* (2006), as follows:

$$\xi = \frac{\beta_f}{(H_0/L_0)^{1/2}} \tag{1}$$

$$\langle\eta\rangle = 0.35\beta_f(H_0L_0)^{1/2} \tag{2}$$

$$R_2 = 1.1\left\{0.35\beta_f(H_0L_0)^{1/2} + \frac{1}{2}\left[H_0L_0(0.563\beta_f^2 + 0.004)\right]^{1/2}\right\} \tag{3}$$

Table 1. *Attributes of hourly wave data during berm erosion experiments. LST = local standard time.*

Survey Date	Time (LST)	H_{mo} (m)	T_p (s)	ξ	$\langle\eta\rangle$ (m)[a]	$\langle\eta\rangle$ (m)[b]	R_2 (m)[a]
21 February 2012	1800	0.52	11.5	0.30	0.054	0.088	0.426
21 February 2012	1900	0.50	11.4	0.30	0.053	0.085	0.414
21 February 2012	2000	0.58	11.8	0.29	0.059	0.099	0.462
7 March 2012	1700	1.13	11.5	0.27	0.107	0.192	0.664
7 March 2012	1800	1.22	11.4	0.26	0.110	0.207	0.684
7 March 2012	1900	1.09	11.4	0.27	0.104	0.185	0.647
20 March 2012	1600	0.59	11.5	0.37	0.077	0.100	0.480
20 March 2012	1700	0.63	11.4	0.36	0.079	0.107	0.492
20 March 2012	1800	0.52	12.4	0.43	0.078	0.088	0.486

[a] Stockdon *et al*. (2006) formula.
[b] Guza and Thornton (1981) formula.

where β_f is the foreshore beach slope and H_0 and L_0 represent the deepwater wave height and length, respectively. An additional setup estimate was computed as follows (Guza and Thornton, 1981):

$$\langle\eta\rangle = 0.17H_s \quad (4)$$

where H_s represents the significant wave height at the 10 m depth. The shoaling coefficient, $K_s = H_s/H_0$, was computed to be 1.028 (nearly unity) based on the wave periods shown in Table 1 using the University of Delaware online wave calculator (Dalrymple, 2013); for this study, wave heights at 10 m depths were used for all setup and runup calculations. Additionally, linear wave theory was used to compute the deepwater wavelength. Average wave attributes corresponding to the time of berm erosion are shown in Table 2.

Wave Runup Observations

Time-lapse photography and georeferenced TLS intensity data enabled direct observation of wave runup, because wetted beach sand produces a low-signal intensity. By visually matching time-lapse photography with TLS data, a threshold of 10 iu was found to outline the wet/dry interface indicative of the maximum runup over the time scale of the scan. The reflected laser intensity for dry sand was found to be generally greater than 12 iu. Hence, the maximum elevation of beach face TLS points (the scan region immediately upcoast and downcoast of the berm) with an intensity less than 10 iu was taken as an indicator of maximum runup elevation, which we denote R_0. Measurement uncertainty is estimated to be <3 cm based on differences in runup measurements achieved by varying the intensity cutoff by ± 4 iu around the 10 iu limit.

RESULTS

The fit of front scan to back scan data was evaluated by comparing point elevations in the region of overlap between the two scans, generally on the beach inland of the berm. These data correspond to initial conditions prior to berm erosion. Beach elevations were sampled at 30 points within the overlap zone. For berm survey 1, height differences average 6 mm. For surveys 2 and 3, height differences average 9 mm and 7 mm, respectively. These values correspond to the expected TLS instrument scanning accuracy at 100 m distances.

Relative and absolute vertical root-mean-square errors (VRMSE) of the full TLS returns are presented in Table 3 for each berm. These data show that performance of the TLS scanner was consistent across the three scanning dates, with relative and absolute errors in the range of 2–3 cm, despite significant differences in environmental conditions. Specifically, windy conditions on 7 March 2012 ($\sim$9.4 m/s) caused visible aerosols and occasional vibrations of the pier with strong gusts. Both of these effects may alter light transmission and reception; the accuracy data, however, provide strong evidence that adverse environmental conditions did not degrade the quality of the scans.

Table 2 shows that the three berms experienced a consistent wave period of 11.5 s, but the wave height for berm 2 (1.2 m) was approximately two times those of berms 1 and 3 (0.5–0.6 m). Table 2 also shows that the Iribarren number was less than 0.4 for each case, corresponding to spilling breakers in the surf zone.

Observations and time-lapse photography reveal a basic, qualitative description of berm erosion. Wave breaking occurred *ca*. 50–100 m offshore of the berm, resulting in irregular bores moving through the swash zone and running up and down the foreshore, similar to the swash regime described by Sallenger (2000). With the rise of the tide, runup eventually reached the toe of the berm, analogous to Sallenger's collision regime (Sallenger, 2000) and causing localized soil saturation and slumping. The slumping process began slowly and accelerated as the berm was increasingly exposed to wave energy (shallow bores) and toe inundation from the rising tide.

Table 2. *Wave attributes associated with the time of berm erosion.*

Survey Date	Time (LST)	H_s (m)	T_p (s)	ξ	$\langle\eta\rangle$ (m)[a]	$\langle\eta\rangle$ (m)[b]	R_2 (m)[a]
21 February 2012	1800–1900	0.51	11.5	0.30	0.054	0.087	0.420
7 March 2012	1700–1800	1.18	11.5	0.26	0.109	0.200	0.674
20 March 2012	1600–1700	0.61	11.5	0.37	0.078	0.104	0.486

[a] Stockdon *et al*. (2006) formula.
[b] Guza and Thornton (1981) formula.

Table 3. *DTM errors (VRMSE) for each scan day.*

Survey Date	GPS Points	Relative Error (m)	GPS Error (m)	Absolute Error (m)
21 February 2012	23	0.025	0.014	0.029
7 March 2012	50	0.022	0.014	0.026
20 March 2012	25	0.027	0.014	0.030
Average	33	0.025	0.014	0.028

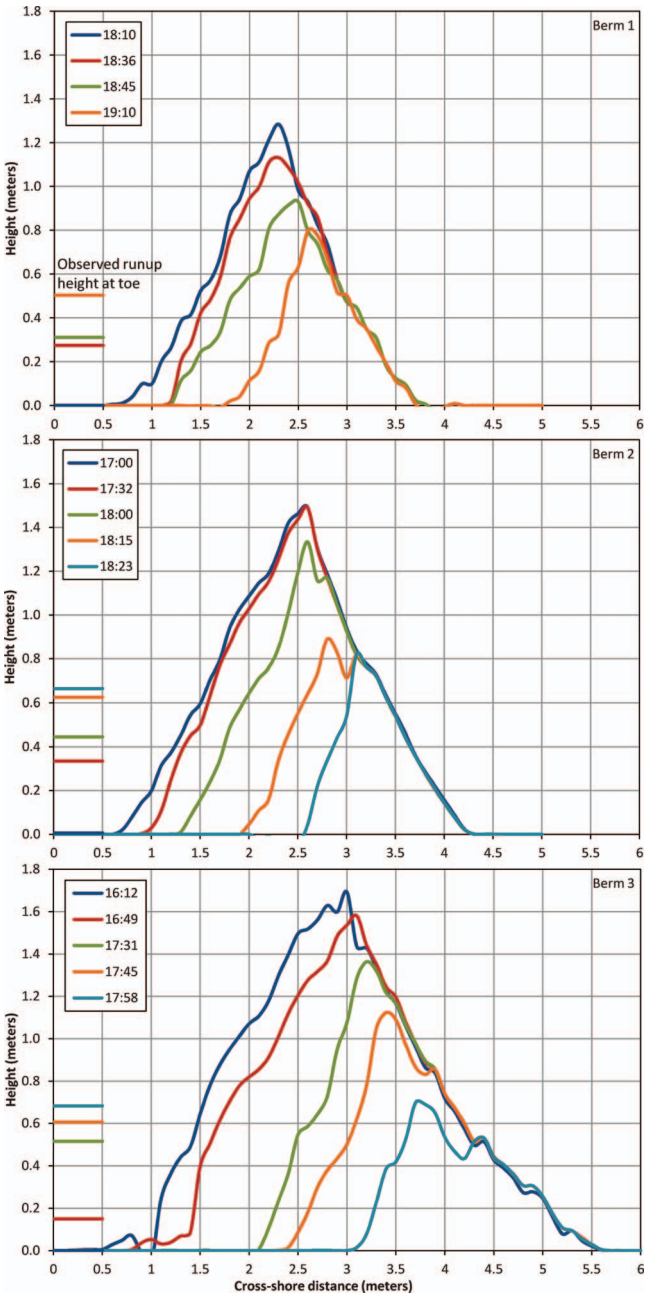

Figure 8. The berm cross-sectional geometry maintained a consistent shape as it was eroded. The height of the observed runup, relative to the initial height of the berm toe, indicates that the berm was eroded while only its toe was initially exposed to the rising tide and waves. (Color for this figure is available in the online version of this paper.)

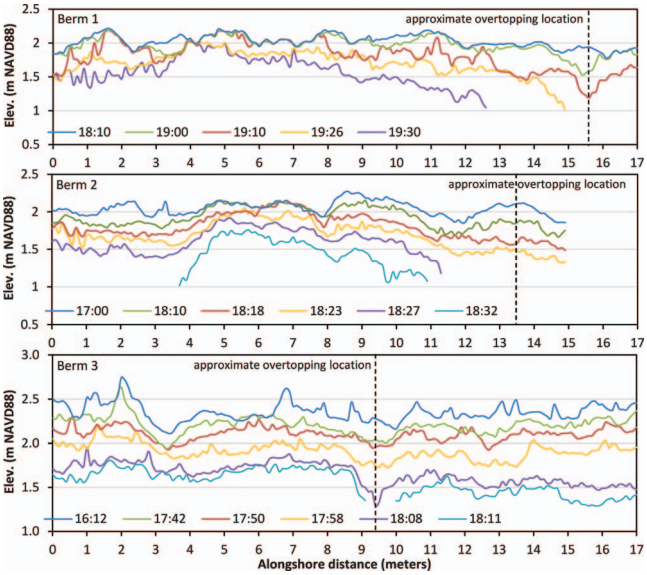

Figure 9. The alongshore variability in berm crest elevation shows that berms 1 and 2 were first overtopped near the end of the central berm section, while Berm 3 was overtopped near the center. The location of initial overtopping does not correspond to an initial low point in the berm. (Color for this figure is available in the online version of this paper.)

In turn, avalanching of relatively dry sand down the angle of repose was observed as the toe was eroded. Hence, over time the face of the berm retreated and the crest height was lowered with every avalanche that extended to the berm crest. Figure 8 presents cross-shore profiles of berm height at overtopping locations from the gridded TLS data. The height of the observed runup is also shown in Figure 8, relative to the height of the berm toe. Note that the dynamic evolution of berm cross-sectional shape was consistent across all three berm prototypes: a gradual reduction in size of a triangular geometry whereby the side slopes remained constant and the left base was translated inland.

Figure 9 presents the alongshore profiles of the central portion of the berm crest. These profiles reveal the irregular initial shape that results from the construction process and the downward progression of berm height resulting from the rising tide and wave action. The alongshore patterns of erosion differed across the three berm experiments. With berms 1 and 2, the ends of the central berm section lowered faster than the middle portion of the central section. In contrast, the central berm crest of berm 3 was lowered relatively uniformly in the alongshore direction. Figure 9 denotes the location of initial overtopping in all three cases, as determined by a review of time-lapse photography. It is noted that overtopping does not occur at the initial berm minima (*i.e.* following construction); the overtopping point is an emergent feature.

Figure 10 shows the coevolution of numerous system attributes. Figures 10a, b, and c (corresponding to berms 1, 2, and 3) show data on elevation (top) and berm erosion (bottom). The elevations shown include average crest elevation, crest elevation at the observed location of overtopping, average toe

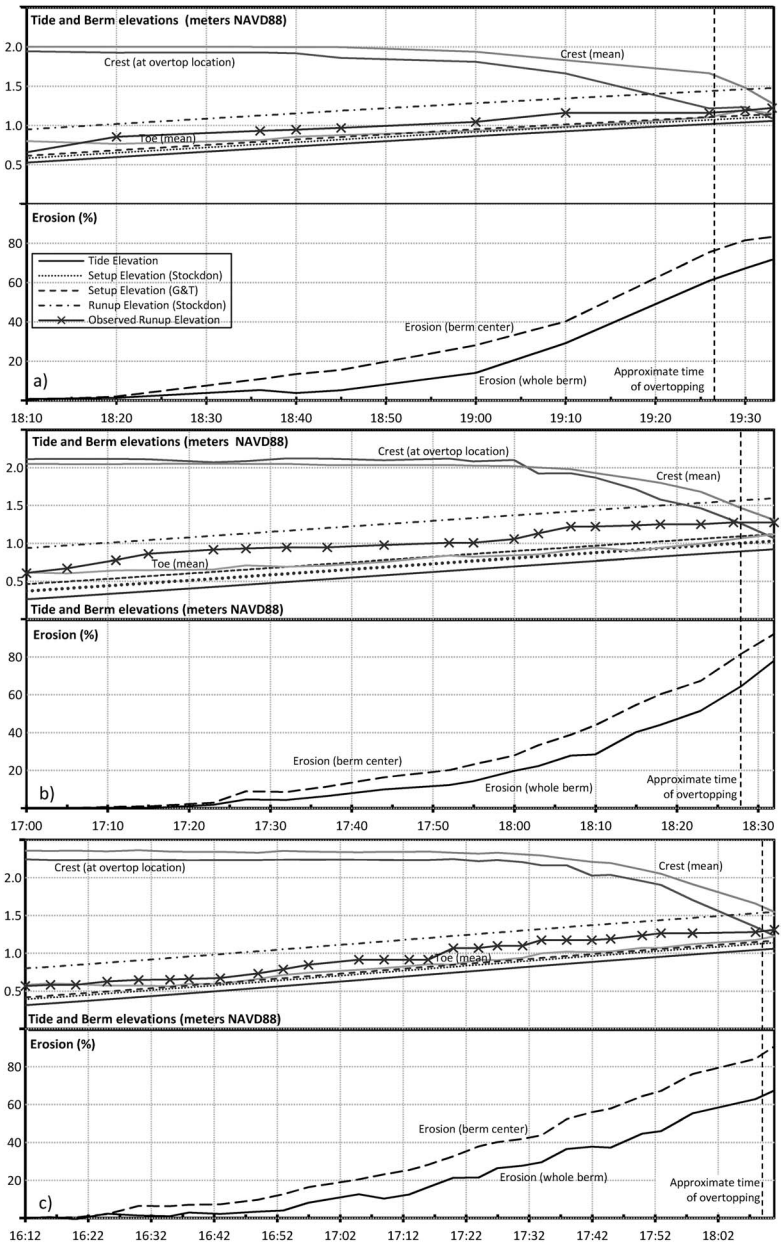

Figure 10. With the rising at a steady rate, the rate of berm erosion progressively increases. The pattern is repeated over three experiments, as shown for (a) berm 1, (b) berm 2, and (c) berm 3. The central berm section erodes faster than the whole berm since the wings of the berm are further ashore, as shown in Figure 2. Note that the observed runup (blue line) matches the crest elevation (red line) at the moment of initial overtopping.

elevation, offshore tide elevation h, the setup elevation estimate ($\langle\eta\rangle + h$), the 2% runup elevation estimate ($R_2 + h$), and the observed runup elevation ($R_0 + h$). Cumulative erosion is shown for the central berm section and for the whole berm (including berm wings), as measured by the berm DTM. The time of initial overtopping is indicated by a vertical dashed line.

Several basic observations can be reported that apply to all three berm experiments. First, the tide rise is nearly linear in time, while the berm crest elevation and cumulative erosion are nonlinear. Both respond slowly at first and then more rapidly approaching the moment of failure.

Second, setup and runup estimates rise nearly linearly in time with the tide, but observed beach runup exhibits variability that departs from a simple linear trend. The observed runup is consistently lower than estimated runup based on Equation (3). The average deviation of computed *vs*. observed runup is 23 cm, 26 cm, and 23 cm for berms 1, 2, and 3, respectively.

Third, the separation between the average crest elevation and elevation at the overtopping location increases over time, indicating an accelerating breaching process similar to other types of embankment failures (*e.g.*, Wu *et al.*, 2011).

Fourth, overtopping occurred *ca.* 60–90 minutes before the observed beach runup elevation attains the elevation of the initial average berm crest (not shown in Figure 10 because it is outside of scale) and 30–60 minutes before the estimated runup elevation attains the initial average berm crest elevation. Average berm crest elevation is lowered by erosion of the berm toe and avalanching, suggesting that berm erosion may be more highly dependent on water level than overtopping.

Fifth, overtopping occurred when the central berm was 75%–80% eroded and the whole berm was 60%–65% eroded by volume.

Finally, eroded sediment was visually observed slumping in the seaward direction, and it appeared to spread out smoothly based on time-lapse photography. However, a precise characterization of foreshore sediment redistribution was not possible because the flooded conditions prevented TLS measurements.

DISCUSSION

The TLS system and time-lapse photography are clearly valuable for investigations of berm dynamics. However, the TLS system used here required an hour or two to set up (including spheres, RTK-GPS ground control points, *etc.*), and two scans were required to characterize the initial conditions (front and back). Assuming that a rapid scan using a mobile platform would be of interest for assessing initial beach profile and informing coastal flood models, and that access to the ocean side of berms is typically not possible, two issues are explored further: (1) Is a single back scan sufficient for mapping the berm crest elevation (recognizing that berm slopes are approximately equal on opposite sides)? (2) Could a coarser point spacing be used to minimize the required scanning time without sacrificing overall accuracy?

Figure 11 presents initial berm crest elevations as determined by the back scan *vs.* the combined (front-back) scans, and it reveals a high degree of coherency. The average vertical error between the two profiles was 0.03 m, 0.04 m, and 0.03 m (RMSE) for berms 1, 2, and 3, respectively, which is within the absolute error of the TLS measurements. Original point cloud data contained occasional spikes in berm elevation from birds on the berm crest. If the TLS data were filtered to remove false hits, the errors would decrease even further.

To answer the second question, additional 7.5 cm resolution berm DTMs were computed using the same interpolation procedure (IDW) but with fewer LIDAR points. DTMs were computed by thinning the original LIDAR point clouds using a modulo operation, leaving only every second, third, fourth, fifth, or sixth point in the LIDAR point cloud. Analysis of the thinned point clouds showed the sampling of points was evenly distributed. Height differences between the undersampled and original DTMs were then measured to compute the undersampling error (VRMSE), which is shown in Figure 12. This shows that the undersampling error is increased as the point density decreases, which is the expected response. We note that the total point density varies from *ca.* 160 m^{-2} to 240 m^{-2} across the three prototype berms due to differences in the distance between the scanner and the berm. Figure 12 also shows the absolute error associated with the TLS data, 2.9 cm VRMSE, indicating that a point density of *ca.* 70–100 m^{-2} or greater is required for the undersampling error to be equal or less than the absolute error of the TLS data. Hence, the TLS scanner setting (7.5 cm) could only be increased to about 10 cm before the berm DTM errors increased beyond the accuracy of individual TLS point heights. A point spacing of 10 cm or finer is thus recommended for future berm-scanning studies.

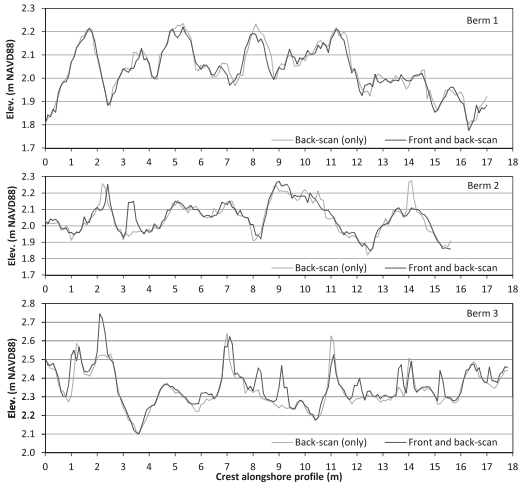

Figure 11. The alongshore characterization of berm crest elevation is closely approximated by a back scan (light gray line), compared with a point cloud based on front and back scans (dark gray line).

In the next section, a regression analysis of erosion is presented with respect to several alternative (dimensionless) water heights. The heights include the Newport tide height, the Los Angeles tide height, the setup elevation based on Stockdon *et al.* (2006) (Equation [2]) and Guza and Thornton (1981) (Equation [4]), the runup elevation based on Stockdon *et al.* (2006) (Equation [3]), and the elevation corresponding to the observed runup.

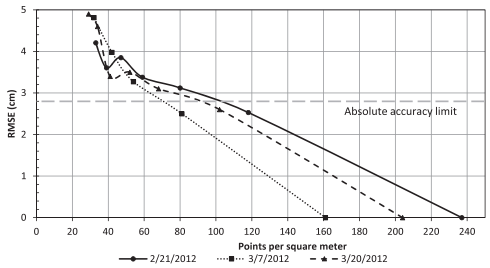

Figure 12. The accuracy of the DTM depends on the density of point cloud data, and by using a minimum of 100 points/m^2, the DTM error associated with the point density remains smaller than the absolute accuracy of the elevation data.

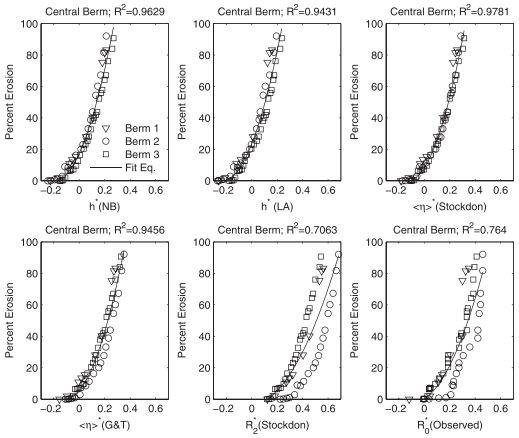

Figure 13. Cumulative erosion of the berm over three experiments correlates well ($R^2 > 0.94$) with dimensionless tide and setup elevations, and it is poorly correlated ($R^2 < 0.77$) with dimensionless runup elevations. Cumulative erosion correlates best with the dimensionless setup elevation based on the formula of Stockdon *et al*. (2006).

Regression of Berm Erosion Data

Several dimensionless water heights were computed for erosion regression analysis. Dimensional water heights are measured relative to the initial toe elevation Z_0 and non-dimensionalized water heights by the initial berm height B_0, which represents the difference between the initial crest and toe elevations. Each dimensionless water height can be interpreted as the fractional height by which the berm is flooded. The dimensionless tide height is based on tide elevation h, as follows:

$$h^* = \frac{h - Z_0}{B_0} \tag{5}$$

where the superscript * denotes a dimensionless variable. The dimensionless wave setup is given by

$$\langle \eta \rangle^* = \frac{h + \langle \eta \rangle - Z_0}{B_0} \tag{6}$$

the dimensionless wave runup is given by

$$R_2^* = \frac{h + R_2 - Z_0}{B_0} \tag{7}$$

and a similar expression is used for the dimensionless observed runup:

$$R_0^* = \frac{h + R_0 - Z_0}{B_0} \tag{8}$$

Figure 13 shows the erosion data for the central section of each berm. Cumulative erosion is shown *vs*. each of the dimensionless heights; also shown is the least-squares fit of a quadratic model of the following form:

$$y = \begin{cases} a(x - x_0) + b(x - x_0)^2 & x \geq x_0 \\ 0 & x < x_0 \end{cases} \tag{9}$$

where x represents the abscissa (dimensionless water level) and y represents the ordinate (cumulative berm erosion expressed as a percentage). The quadratic model given by Equation (9) is fit subject to the constraint $y \geq 0 \; \forall x$ to guarantee a monotonic increase in cumulative erosion with increasing water levels.

Fit parameters are shown in Table 4, and the results are plotted in Figure 13. All of the regressions yield a high value for the coefficient of determination ($R^2 > 0.7$), and the fit is generally better for the central berm data than the whole berm data. The dimensionless Stockdon setup ($\langle \eta \rangle^*$) represents the best fit for both the central berm data ($R^2 = 0.978$) and the whole berm data ($R^2 = 0.948$), but the fit based on all tide and setup heights is excellent ($R^2 > 0.89$). On the other hand, poorest fit ($R^2 \sim 0.7$) is associated with dimensionless runup heights (R_2^* and R_0^*). Figure 13 suggests the relatively poor fit is attributable to berm 2, which is offset from the other two berms in the panels corresponding to observed runup height, predicted runup height, and the Guza and Thornton (1981) setup height. Berm 2 experienced the largest waves of the three test cases, so the comparatively weak regression with runup may indicate that waves are not controlling erosion. Instead these results suggest that berm erosion is controlled by its degree of submergence, best indicated by the Stockdon *et al*. (2006) setup height, and they leave open the possibility that wave action is important for agitating or destabilizing the berm toe and moving material away down the shore face. Previous work has also indicated that erosion is linked to water level (Basco and Shin, 1996).

The berms were observed to be stable after construction, and erosion only began after water came in contact with the berm. Therefore, the fit model given by Equation (9) is designed with a parameter representing the threshold for erosion, x_0. Depending on the regression, x_0 was found to vary from –0.23 to 0.074, which can be interpreted as a water level 23% below or 7.4% above the toe of the berm, relative to the initial height of the berm. Using the scaled Stockdon *et al*. (2006) water level, $x_0 = -0.131$, indicating that berm erosion begins when the setup elevation is about 13% below the berm toe elevation, relative to the initial berm height. Previously it was noted that berm overtopping occurred when the central berm section was 75%–80% eroded. Based on Figure 10, this occurs when the scaled Stockton *et al*. (2006) water level is in the range 0.25–0.30. This indicates that the erosion is initiated and completed as the water level rises from 13% below to 25%–30% above the initial toe elevation, respectively, relative to the height of the berm.

This simple scaling was exceptionally consistent over all three berms and may represent a rapid method of predicting triangular berm failure onset and, by extension, flood risk for a specific site under similar wave conditions. It is important to note, however, that the regression equations may not be applicable at other locations, to other berm geometries, or even to the same site under different wave conditions. For example, the Iribarren number was less than 0.43 for all experiments, which corresponds to spilling breaker types, and the erosion mechanism may be different when other breaker types are present.

Table 4. *Quadratic model parameters and coefficient of determination.*

	Central Berm				Whole Berm			
Predictor	x_0	a	b	R^2	x_0	a	b	R^2
h^* (NB)	−0.193	2.510	453.0	0.963	−0.138	−0.320	467.5	0.918
h^* (LA)	−0.230	−0.302	447.2	0.943	−0.175	0.624	447.9	0.889
$\langle\eta\rangle^{*a}$	−0.131	0.000	484.4	0.978	−0.068	−0.463	526.0	0.948
$\langle\eta\rangle^{*b}$	−0.113	−0.906	441.6	0.946	−0.044	−0.850	490.3	0.934
$R^*_2{}^a$	−0.159	−54.32	193.6	0.706	0.074	−10.10	213.7	0.713
$R^*_2{}^c$	0.000	54.799	263.7	0.764	0.000	4.502	288.218	0.736

NB = Newport Beach, LA = Los Angeles.
[a] Stockdon *et al.* (2006) formula.
[b] Guza and Thornton (1981) formula.
[c] Observation based on LIDAR intensity data.

CONCLUSIONS

TLS delivers an accurate model of berm geometry. A comparison with ground control points reveals an average error of 2.5 cm (VRMSE) over three berm prototypes and a high level of consistency across prototypes, despite one case of strong, gusty winds that represented more challenging scanning conditions. TLS also provides signal intensity data that is strongly linked to moisture content.

The TLS was operated with a point spacing of 7.5 cm at a distance of 100 m, leading to average point densities of 160–240 m^{-2}. Differences across the three berms were the result of slightly different scanner and berm positions across the three prototypes. Analysis of the TLS data suggests that berm geometry could be mapped at the same level of accuracy with a resolution as large as 10 cm. At this resolution, uncertainty in the berm elevation associated with undersampling would be equal to the expected error of the TLS data compared with the ground control points. This result suggests that there is relatively little margin for increasing the LIDAR point cloud spacing without increasing the absolute error of the berm height data beyond *ca.* 3 cm.

Berm crest elevations estimated using only back scan data compare favorably with berm crest elevations estimated from combined front and back scans. Recognizing that a rapid scan of beach berms could help inform coastal flood prediction models, scanning from the back side may represent an efficient proxy for berm elevation or maximum beach crest for rapid assessment of overtopping probability.

Continuous LIDAR scanning and time-lapse photography of anthropogenic beach berms exposed to a rising tide and waves leads to a four-dimensional empirical model of berm dynamics. For the site considered and the three days tested, a relatively simple erosion pattern was observed: As runup first strikes the toe of the berm, berm sediment saturates and begins to slump. With continued slumping and offshore sediment transport by wave action, avalanching occurs down the angle of repose, causing the retreat of the berm face inland and a progressive loss of sand and lowering of the crest elevation. The rise of the tide was nearly linear in time over the duration of berm erosion, and the erosion and lowering of the beach crest was nonlinear with time, characterized first by a gradual and then by a rapid change. A dimensionless setup elevation representing the fractional submergence of the berm is identified as a good predictor of cumulative berm erosion under the test conditions. Across the three berm experiments, erosion of the central berm section begins when the setup elevation is about 13% below the toe of the berm relative to the initial berm height, and the berm is overtopped when the setup elevation is 25%–30% of the initial berm height and the berm is 75%–80% eroded by volume.

ACKNOWLEDGMENTS

This work was supported by the Infrastructure Management and Extreme Events program of the National Science Foundation (CMMI-1129730) and was made possible by the gracious cooperation of City of Newport Beach personnel who authorized access to the site and provided equipment and operators for constructing the beach berms. We also thank the Orange County Sanitation District for support of the research vessel *Nerissa* and its crew for instrument deployment and retrieval, and Ed Beighley and Ken Walsh of San Diego State University for making the GX3D TLS available for berm scanning.

LITERATURE CITED

Barber, D.M. and Mills, J.P., 2007. Vehicle based waveform laser scanning in a coastal environment. *International Archive of Photogrammetry, Remote Sensing and Spatial Information Sciences,* 36(part 5), C55.

Basco, D.R. and Shin, C.S., 1996. Dune damage curves and their use to estimate dune maintenance costs. *Coastal Engineering Proceedings,* 1(25), 2969–2981.

Bates, P.D., 2012. Integrating remote sensing data with flood inundation models: How far have we got? *Hydrological Processes,* 26(16), 2515–2521.

Bates, P.D.; Dawson, R.J.; Hall, J.W.; Horritt, M.S.; Nicholls, R.J.; Wicks, J., and Hassan, M.A.A.M., 2005. Simplified two-dimensional numerical modelling of coastal flooding and example applications. *Coastal Engineering,* 52(9), 793–810.

Bitenc, M.; Lindenbergh, R.; Khoshelham, K., and Van Waarden, A.P., 2011. Evaluation of a LiDAR land-based mobile mapping system for monitoring sandy coasts. *Remote Sensing,* 3(7), 1472–1491.

Brock, J.; Wright, C.; Sallenger, A.; Krabill, W., and Swift, R., 2002. Basis and methods of NASA Airborne Topographic Mapper lidar surveys for coastal studies. *Journal of Coastal Research,* 18(1), 1–13.

Brown, J.D.; Spencer, T., and Moeller, I., 2007. Modeling storm surge flooding of an urban area with particular reference to modeling uncertainties: A case study of Canvey Island, United Kingdom. *Water Resources Research,* 43(6), W06402.

Bruun, P., 1983. Beach scraping—Is it damaging to beach stability? *Coastal Engineering,* 7(2), 167–173.

Carley, J.T.; Shand, T.D.; Coghlan, I.R.; Blacka, M.J.; Cox, R.J.; Littman, A.; Fitzgibbon, B.; McLean, G., and Watson, P., 2010. Beach scraping as a coastal management option. *Proceedings of the 19th NSW Coastal Conference* (Batemans Bay, NSW, Australia). http://coastalconference.com/2010/papers2010/James%20Carley%20full%20paper.pdf.

Cayan, D.R.; Bromirski, P.D.; Hayhoe, K.; Tyree, M.; Dettinger, M.D., and Flick, R.E., 2008. Climate change projections of sea level extremes along the California coast. *Climatic Change,* 87(Suppl 1), S57–S73.

Chust, G.; Galparsoro, I.; Borja, A.; Franco, J., and Uriarte, A., 2008. Coastal and estuarine habitat mapping, using LIDAR height and intensity and multi-spectral imagery. *Estuarine, Coastal and Shelf Science,* 78(4), 633–643.

Clark, R., 2005. *Hurricane Dennis Supplemental Damage Assessment Report: Impact of Hurricane Dennis on Dog Island and Discussion of Post-Storm Recovery Responses*. Florida: Florida Department of Environmental Protection, Division of Water Resource Management, Bureau of Beaches and Coastal Systems. http://bcs.dep.state.fl.us/reports/dog_island.pdf.

Dalrymple, R., 2013. *University of Delaware Wave Calculator*. www.coastal.udel.edu/faculty/rad/wavetheory.html.

Dawson, R.J.; Dickson, M.E.; Nicholls, R.J.; Hall, J.W.; Walkden, M.J.A.; Stansby, P.; Mokrech, M.; Richards, J.; Zhou, J.; Milligan, J.; Jordan, A.; Pearson, S.; Rees, J.; Bates, P.; Koukoulas, S., and Watkinson, A., 2009. Integrated analysis of risks of coastal flooding and cliff erosion under scenarios of long term change. *Climatic Change,* 95(1–2), 249–288.

Feagin, R.A.; Williams, A.M.; Popescu, S.; Stukey, J., and Washington-Allen, R.A., 2014. The use of terrestrial laser scanning (TLS) in dune ecosystems: The lessons learned. *Journal of Coastal Research,* 30(1), 111–119.

Figlus, J.; Kobayashi, N.; Gralher, C., and Iranzo, V., 2011. Wave overtopping and overwash of dunes. *Journal of Waterway, Port, Coastal and Ocean Engineering,* 137(1), 26–33.

Fisher, J.S.; Overton, M.F., and Chisholm, T., 1986. Field measurements of dune erosion. *Coastal Engineering Proceedings,* 1(20), 1107–1115.

Flick, R.E., 1998. Comparison of California tides, storm surges and mean sea level during the El Niño winters of 1982–83 and 1997–98. *Shore and Beach,* 66(3), 7–11.

Gallien, T.W.; Barnard, P.; van Ormondt, M.; Foxgrover, A., and Sanders, B.F., 2013. A Parcel-scale coastal flood forecasting prototype for a Southern California urbanized embayment. *Journal of Coastal Research,* 29(3), 642–656.

Gallien, T.W.; Sanders, B.F., and Flick, R.E., 2014. Modeling urban coastal flooding from wave-driven beach overtopping: Field validation and uncertainty analysis. *Coastal Engineering*. http://dx.doi.org/10.1016/j.coastaleng.2014.04.007.

Gallien, T.W.; Schubert, J.E., and Sanders, B.F., 2011. Predicting tidal flooding of urbanized embayments: A modeling framework and data requirements. *Coastal Engineering,* 58(6), 567–577.

Guza, R.T. and Thornton, E.B., 1981. Wave set-up on natural beaches. *Journal of Geophysical Research,* 86(C5), 4133–4137.

Hanson, S.; Nicholls, R.; Ranger, N.; Hallegatte, S.; Corfee-Morlot, J.; Herweijer, C., and Chateau, J., 2011. A global ranking of port cities with high exposure to climate extremes. *Climate Change,* 104(1), 89–111.

Harley, M.D. and Ciavola, P., 2013. Managing local coastal inundation risk using real-time forecasts and artificial dune placements. *Coastal Engineering,* 77(00), 77–90.

Heberger, M.; Cooley, H.; Herrera, P.; Gleick, P.H., and Moore, E., 2009. *The Impacts of Sea-Level Rise on the California Coast*. Oakland: Pacific Institute, 101p.

Knowles, N., 2010. Potential inundation due to rising sea levels in the San Francisco Bay region. *San Francisco Estuary & Watershed Science*, 8(1). http://escholarship.org/uc/item/8ck5h3qn.

Kratzmann, M.G. and Hapke, C.J., 2012. Quantifying anthropogenically driven morphologic changes on a barrier island: Fire Island National Seashore, New York. *Journal of Coastal Research,* 28(1), 76–88.

Laudier, N.A.; Thornton, E.B., and MacMahan, J., 2011. Measured and modeled wave overtopping on a natural beach. *Coastal Engineering,* 58(9), 815–825.

Martinelli, L.; Zanuttigh, B., and Corbau, C., 2010. Assessment of coastal flooding hazard along the Emilia Romagna littoral, IT. *Coastal Engineering,* 57(11–12), 1042–1058.

McNinch, J.E. and Wells, J.T., 1992. Effectiveness of beach scraping as a method of erosion control. *Shore and Beach,* 60(1), 13–20.

National Research Council Staff, 2009. *Mapping the Zone. Improving Flood Map Accuracy*. Washington, D.C.: National Academies Press, 122p.

Nicholls, R.J., 2010. Impacts of and responses to sea-level rise. *In*: Church, J.A.; Woodworth, P.L.; Aarup, T., and Wilson, W.W. (eds.), *Understanding Sea-Level Rise and Variability*. Chichester, UK: Wiley-Blackwell, pp. 17–51.

Nicholls, R.J., 2011. Planning for the impacts of sea level rise. *Oceanography,* 24(2), 144–157.

Nobrega R.; Quintanilha J.A., and C.G.,O'Hara, 2007. A noise-removal approach for Lidar intensity images using anisotropic diffusion filtering to preserve object shape characteristics. *Proceedings of the ASPRS 2007 Annual Conference* (Tampa, Florida), pp. http://www.asprs.org/a/publications/proceedings/tampa2007/toc.pdf.

Orange County Department of Public Works, 2014. http://media.ocgov.com/gov/pw/survey/services/ocrtn.asp.

Purvis, M.J.; Bates, P.D., and Hayes, C.M., 2008. A probabilistic methodology to simulate future coastal flood risk due to sea level rise. *Coastal Engineering,* 55(00), 1062–1073.

Roelvink, D.; Reniers, H.M.; Van Dongeren, J.A.; van Thiel de Vries, J.S.M.; McCall, R.T., and Lescinski, J., 2009. Modelling storm impacts on beaches, dunes and barrier islands. *Coastal Engineering,* 56(11–12), 1133–1152.

Rogers, J.; Hamer, B.; Brampton, A.; Challinor, S.; Glennerster, M.; Brenton, P., and Bradbury, A., 2010. *Beach Management Manual,* 2nd edition. London: CIRIA, 860p.

Sallenger, A.H., 2000. Storm impact scale for barrier islands. *Journal of Coastal Research,* 16(3), 890–895.

Sallenger, A.H., Jr.; Krabill, W.B.; Swift, R.N.; Brock, J.; List, J.; Hansen, M.; Holman, R.A.; Manizade, S.; Sontag, J.; Meredith, A.; Morgan, K.; Yunkel, J.K.; Frederick, E.B., and Stockdon, H., 2003. Evaluation of airborne topographic Lidar for quantifying beach changes. *Journal of Coastal Research,* 19(1), 125–133.

Sampson, C.C.; Fewtrell, T.J.; Duncan, A.; Shaad, K.; Horritt, M.S., and Bates, P.D., 2012. Use of terrestrial laser scanning data to drive decimetric resolution urban inundation models. *Advances in Water Resources,* 41(00), 1–17.

Smith, R.A.E.; Bates, P.D., and Hayes, C., 2012. Evaluation of a coastal flood inundation model using hard and soft data. *Environmental Modelling and Software,* 30(00), 35–46.

Stockdon, H.F.; Holman, R.A.; Howd, P.A., and Sallenger, A.H., 2006. Empirical parameterization of setup, swash and runup. *Coastal Engineering* 53(00), 573–588.

Strauss, B.H.; Ziemlinski, R.; Weiss, J.L., and Overpeck, J.T., 2012. Tidally adjusted estimates of topographic vulnerability to sea level rise and flooding for the contiguous United States. *Environmental Research Letters,* 7(1), 014033.

Tebaldi, C.; Strauss, B.H., and Zervas, C.E., 2012. Modelling sea level rise impacts on storm surges along US coasts. *Environmental Research Letters,* 7(1), 014032.

Tye, R.S., 1983. Impact of Hurricane David and mechanical dune restoration on Folly Beach, South Carolina. *Shore and Beach,* 51(2), 3–9.

van Rijn, L., 2009. Prediction of dune erosion due to storms. *Coastal Engineering,* 56(4), 441–457.

Vossman, G. and Maas, H.G., 2010. *Airborne and Terrestrial Laser Scanning*. Dunbeath, Scotland, U.K.: Whittles Publishing, 318p.

Vousdoukas, M.I.; Ferreira, O.; Almeida, L.P., and Pacheco, A., 2012. Toward reliable storm-hazard forecasts: XBeach calibration and its potential application in an operational early-warning system. *Ocean Dynamics,* 62(7), 1001–1015.

Vouskoukas, M.I.; Kirupakaramoorthy, T.; Oumeraci, H.; de la Torre, M.; Wubbold, F.; Wagner, B., and Schimmels, S., 2014. The role of combined laser scanning and video techniques in monitoring wave-by-wave swash zone processes. *Coastal Engineering,* 83(1), 150–165.

Wadey, M.P.; Nicholls, R.J., and Hutton, C., 2012. Coastal flooding in the Solent: An integrated analysis of defences and inundation. *Water,* 4(2), 430–459.

Wells, J.T. and McNinch, J., 1991. Beach scraping in North Carolina with special reference to its effectiveness during Hurricane Hugo. *Journal of Coastal Research,* Special Issue No. 8, pp. 249–261.

Wu, W.M.; Altinakar, M.S.; Al-Riffai, M.; Bergman, N.; Bradford, S.F.; Cao, Z.X.; Chen, Q.J.; Constantinescu, S.G.; Duan, J.G.; Gee, D.M.; Greimann, B.; Hanson, G.; He, Z.G.; Hegedus, P.; van Hoestenberghe, T.; Huddleston, D.; Hughes, S.A.; Imran, J.; Jia, Y.F.; Jorgeson, J.D.; Kahawita, R.; Klumpp, C.C.; Lai, Y.; Langendoen, E.J.; Liu, S.E.L.; Moreda, F.; Morris, M.; Morvan, H.; Orendorff, B.; Pak, J.; Peeters, P.; Reed, S.; Sanders, B.F.; Scott, S.H.; Soares-Frazao, S.; Song, C.R.; Sutherland, J.; Teal, M.J.; Tsubaki, R.; Wahl, T.L.; Weston, D.M.; Williams, D.T.; Zech, Y., and Zhang, L.M., 2011. Earthen embankment breaching. *ASCE Journal of Hydraulic Engineering,* 137(11), 1549–1564.

Yates, M.L.; Guza, R.T.; Gutierrez, R., and Seymour, R., 2008. A technique for eliminating water returns from lidar beach elevation surveys. *Journal of Atmospheric and Oceanic Technology,* 25(9), 1671–1682.

Zhu, F. and Dodd, N., 2013. Net beach change in the swash zone: A numerical investigation. *Advances in Water Resources,* 53(00), 12–22.